



## Strain-gradient modelling of grain size effects on fatigue of CoCr alloy

Title	Strain-gradient modelling of grain size effects on fatigue of CoCr alloy
Author(s)	Sweeney, Caoimhe A.; O'Brien, Barry J.; Dunne, Fionn P. E.; McHugh, Peter E.; Leen, Sean B.
Publication Date	2014-07-30
Publisher	Elsevier
Repository DOI	<a href="https://doi.org/10.1016/j.actamat.2014.06.044">10.1016/j.actamat.2014.06.044</a>

## Strain-gradient modelling of grain size effects on fatigue of CoCr alloy

C.A. Sweeney<sup>a,\*</sup>, B. O'Brien<sup>b</sup>, F.P.E. Dunne<sup>c</sup>, P.E. McHugh<sup>b</sup>, S.B. Leen<sup>a</sup>

<sup>a</sup>*Mechanical Engineering, College of Engineering and Informatics, National University of Ireland Galway, Ireland*

<sup>b</sup>*Biomedical Engineering, College of Engineering and Informatics, National University of Ireland Galway, Ireland*

<sup>c</sup>*Department of Materials, Imperial College London*

*\*Corresponding author: Tel: +353 (0)91 493020; Fax: +353 (0)91 563991;  
E-mail: c.sweeney4@nuigalway.ie*

### Abstract

A strain-gradient crystal plasticity framework, based on physical dislocation mechanisms, is developed for simulation of the experimentally-observed grain size effect on low cycle fatigue of a CoCr alloy. Finite element models of the measured microstructure are presented for both as-received and heat-treated CoCr material, with significantly different grain sizes. Candidate crystallographic slip based parameters are implemented for prediction of fatigue crack initiation. The measured beneficial effects of fine grain size on both cyclic stress-strain response and crack initiation life are predicted. The build-up of geometrically necessary dislocations due to strain-gradients, leading to grain-size dependent material hardening, is shown to play a key role.

*Keywords:* size effect, fatigue behaviour, crystal plasticity, geometrically necessary dislocations, finite element

## 1. Introduction

It is well established that fatigue damage and fatigue crack initiation (FCI) in metals are sensitive to microstructure [1,2]. Experimental evidence indicates that grain size is a key microstructural feature affecting fatigue performance. Morrison and Moosbrugger [3], for example, presented an experimental study on the fatigue of coarse- and fine-grained polycrystalline nickel, reporting larger stress amplitudes and longer fatigue lives for the fine grain material under strain-controlled plasticity conditions. While fine-grained materials are FCI-resistant, coarse grains have been shown to give an increased threshold stress intensity factor range and, thus, improved resistance to fatigue crack growth [4,5]. Consequently, numerous industrial applications take advantage of the grain size effect, with components designed to have fine-grained surfaces, where FCI is more likely to occur [1], and coarse-grained interiors, for example, to resist crack growth. In the case of micro-scale components, for which microstructural features are comparable in size to component sectional dimensions, such as stents or micro-electro-mechanical devices, FCI typically dominates fatigue life and, therefore, a fine-grained structure is desirable throughout the load-carrying sections [6].

FCI is known to originate within persistent slip bands (PSBs), formed due to the build-up of mobile dislocations during irreversible cyclic slip [2,7]. This paper hypothesises that the key physical basis of the grain size effect in fatigue lies in the development of immobile geometrically necessary dislocations (GNDs) to accommodate curvature of the crystal lattice in response to plastic strain-gradients, which hinder the movement of mobile dislocations. Littlewood and Wilkinson [8] presented an electron back-scatter diffraction study on cyclically deformed Ti-6Al-4V in which lattice rotation was measured and used to identify GND distributions via a cross-correlation technique. The study provided experimental evidence of high GND densities in regions of large strain gradients near grain boundaries

and within grains. Finer-grained microstructures produce higher gradients of plastic strain and, thus, associated regions of increased GND densities. As a result, these regions are thought to experience increased cyclic hardening and, therefore, exhibit reduced plastic slip, improving fatigue performance.

While this paper focuses on manifestation of the grain size effect via strain-gradient plasticity, other size effects can equally influence the fatigue behaviour of metals. Geers et al. [9] categorised size effects into (i) strain-gradient effects, (ii) intrinsic size effects, (iii) statistical size effects and (iv) surface constraint size effects. As previously mentioned, strain-gradient effects result from the storage of GNDs to allow lattice curvature. Intrinsic effects, also known as microstructural size effects, refers to the influence of intrinsic length scales in the microstructure, such as Burger's vector magnitude, obstacle size and spacing, grain size and grain boundary width [10,11]. For example, strengthening due to the Orowan mechanism is dependent on obstacle spacing and, thus, can be classified an intrinsic size effect. Strengthening as a function of grain size due to the pile-up of dislocations at grain boundaries is another such effect (modelled empirically using the Hall-Petch relation). Statistical size effects arise when device or specimen dimensions are comparable to grain size. The mechanical performance of such devices is often dictated by the behaviour of relatively few grains. Hence, features such as crystallographic orientation can significantly affect mechanical performance. Grogan et al. [12] investigated statistical size effects on the performance of stents to develop a series of equations ensuring safe stent design, including a relationship between grain size, strut length and maximum strain. Finally, surface constraints become increasingly important in the presence of a high ratio of surface area to volume. The behaviour of material at an interface or along a free surface can significantly affect the behaviour of a thin specimen, as illustrated by Geers et al. [9].

Nye [13] and later Ashby [14] proposed the storage of GNDs as the mechanism by which strain gradients are accommodated in the crystal lattice. Fleck et al. [15] developed a strain gradient plasticity theory based on dislocation mechanisms, describing the storage of GNDs as a result of strain-gradients, and applied it to torsion of circular section wire. Macroscopic continuum models have since been developed to deal with the presence of strain gradient effects. For example, one study homogenized the behaviour of a weld steel material in finite element (FE) fatigue analyses by assigning strength to homogenisation units based on the empirical Hall-Petch relation and a statistical grain size distribution [16], to circumvent the explicit modelling of strain-gradients in different-sized grains. Taking this a step further, a crystal plasticity (CP) formulation, describing plastic slip on individual slip systems in the crystal lattice, have also been developed to include a Hall-Petch term with a threshold stress for fretting fatigue of Ti-6Al-4V [17–19]. However, more accurate and realistic predictive models require a more fundamental, physically-based approach, based on GND evaluation, to capture lengthscale and, hence grain (and other microstructure) size effects. Various strain-gradient CP formulations, including the work of Fleck et al. [15], have been developed [20–25], via inclusion of hardening mechanisms based on the evolution of GND density. One such CP formulation has been used by Cheong et al. [20] to predict grain size effect on monotonic stress-strain response for copper polycrystals. Ma et al. [22] applied a similar approach to predict the stress field during shearing of an aluminium single crystal, while Dunne and co-workers [25] successfully predicted the measured GND density field near a carbide particle in a nickel single crystal. However, evidence has yet to be presented on strain-gradient CP modelling of the experimentally observed grain size effect on fatigue behaviour.

A key objective of this study is the assessment of fatigue performance, via prediction of fatigue life. Various macro-scale criteria have been developed for assessment of total life fatigue performance, e.g. [26–28]. However, these approaches have limited viability for micro-scale design. Fatigue life ( $N_f$ ) can be decomposed into number of cycles to crack initiation ( $N_i$ ), microstructurally small crack growth, physically small crack growth and long crack growth [2]; the first two are microstructurally-driven processes [1,2], while the latter can be largely predicted via fracture mechanics. Significant scatter is observed in fatigue due to microstructural inhomogeneity, which cannot be captured by macro-scale models. Microstructure-based approaches, e.g. CP modelling, which take into account these inhomogeneities, have the potential to capture scatter in fatigue performance e.g. [29,30]. Microstructure-based fatigue criteria are attractive for the assessment and design of components on the micro-scale. Mura [31] proposed a model for FCI based on the stability of dislocation structures in a PSB, evaluated via an energy balance in a mathematical model for the evolution of dislocation structures. Sangid and co-workers [32–34] adopted a detailed physically-based energy balance approach for FCI in a slip band spanning a grain, including terms to account for applied stress-field, work hardening, formation of dislocation dipole structures, dislocation nucleation at grain boundaries, penetration of grain boundaries by dislocations, and interruption of lattice stacking sequence in the matrix and precipitates. Macro-scale criteria have been adapted for use at the micro-scale. For example, the Smith-Watson-Topper and Fatemi-Socie criteria have been used as fatigue indicator parameters (FIPs) in conjunction with a critical plane approach to predict fatigue life and number of cycles to FCI, respectively, in CP simulations of fretting fatigue [18,19,35,36]. More recently, microstructure-sensitive FIPs have been developed specifically for CP fatigue predictions. One example of this is the effective crystallographic slip parameter presented by Manonukul and Dunne [37], used to successfully predict numbers of cycles to FCI across

both LCF and HCF regimes, for various cyclic loading ratios and temperatures. The applicability of this FIP has been further investigated with strain-gradient CP to predict experimentally-observed FCI for several four-point bending, ferritic steel specimens, with a view to investigating the role of strain-gradients, anisotropic elasticity and plastic slip in FCI [38]. Strong correlation was demonstrated between distributions of the effective crystallographic slip FIP and the experimentally observed crack sites, and the study also revealed a strong correlation between computationally predicted peaks of GND density and experimental FCI sites, suggesting that GND density itself could be employed as an FIP. A crystallographic work parameter has also been developed for use with CP models [39], which addresses the need for stress-strain criteria.

In this study, a physically-based strain-gradient CP methodology is developed and is shown to successfully predict the effect of grain size on both the cyclic stress-strain (hysteresis) and crack initiation fatigue behaviour of a biomedical grade CoCr alloy. LCF test data is presented for both fine-grained (as-received) and coarse-grained (after heat treatment) test specimens of the material, to quantify the effect of grain size on cyclic stress-strain curves and initiation life. The strain-gradient constitutive formulation of [25] is modified through the inclusion of statistically-stored dislocation (accumulation and annihilation) evolution equations. The measured grain morphology statistics are implemented in unit cell FE models of the coarse- and fine-grained materials and combined with the constitutive model for comparison with the measured hysteresis and FCI behaviour, vis-a-vis grain size and strain range effects. A additional novel aspect is the combined use of a damage evolution curve for FCI identification (from experimental damage data) and microstructure-sensitive FIPs, based on crystallographic slip and work, for prediction of crack initiation life.

## 2. Experiments

The material tested is the L605 CoCr alloy, trade-named HAYNES 25 alloy [40], which has a face-centred cubic (fcc) crystal structure [41]. The material was received as a hot-rolled bar, solution-annealed at 1230 °C, with chemical composition of 20 wt% chromium, 15 wt% tungsten, 10 wt% nickel, 3 wt% iron, 1.5 wt% manganese, 0.4 wt% silicon, 0.1 wt% carbon and the balance consisting of cobalt. The test programme includes (i) heat-treatment of the alloy to increase the grain size, (ii) microstructural characterization via microscopy of the as-received and heat-treated material and (iii) mechanical testing of the two material conditions to measure the effect of microstructure on the fatigue behaviour. Some microscopy and mechanical testing of the as-received material were reported in a previous study [30], but are presented here also for comparison.

### 2.1. Heat-treatment and microscopy

Heat-treatment of the L605 material was employed to effect a significant increase in grain size. The initial iterative heat-treatment tests were based on solution annealing temperatures suggested for the L605 alloy [42]. Based on the observed changes in grain size, a final heat-treatment protocol was implemented; this corresponds to annealing at a 1250 °C for 2.5 hours.

Optical microscopy employed for both as-received and heat-treated material, using an etching solution of 100ml HCl and 5ml 30% H<sub>2</sub>O<sub>2</sub>, to discern information on grain size and grain area distributions. Optical micrographs of the as-received and heat-treated material can be seen in Fig. 1(a); the grain sizes were found to be 32 µm and 243 µm, respectively. Twin boundaries are visible in both microstructures, formed during the annealing process. Microscopy images of both transverse and longitudinal cross-sections of the as-received and

heat-treated bar portions revealed no discernible difference in grain structure and, thus, an equiaxed microstructure was inferred for the two conditions. Scanning electron microscopy (SEM) was used to investigate particles in the L605 matrix, including energy dispersive x-ray (EDX) spectroscopy for identification of particle composition, and crystallographic texture, via electron backscatter diffraction (EBSD), for the two material conditions. As reported previously [30], the as-received material contained precipitates with high tungsten and carbon content (relative to the L605 matrix) with a total area fraction of 0.52%. Microscopy of the heat-treated material yielded no signs of precipitates. This is in agreement with a previous study on L605 precipitates [43], which reported that almost no precipitates were visible after heat-treating at temperatures above 1200 °C. EBSD orientation maps, provided in Fig. 1(b) for both the as-received and heat-treated material conditions for views parallel and perpendicular to the central axis of the cylindrical CoCr bar, indicate the absence of crystallographic texture (i.e. random crystallographic orientations) for the two material conditions.

## 2.2. Mechanical testing

The fatigue test program consisted of strain-controlled LCF tests on the as-received and heat-treated materials at strain ranges  $\pm 0.5\%$  and  $\pm 1.0\%$ . The specimen design followed ASTM standards [44] for strain-controlled fatigue; the test rig employed is an Instron 8500 servo hydraulic system with hydraulic grips and V-shaped jaws at a strain rate of  $1.0\% \text{ s}^{-1}$ . The test was stopped in each case when a 30% drop in maximum load was observed following stabilisation of initial cyclic hardening.

## 3. Computational framework

This section describes the development of the FE model, including both strain-gradient CP constitutive formulation and microstructure geometry, used to simulate the LCF tests of Section 2 for the as-received and heat-treated materials.

### 3.1. Crystal plasticity constitutive model

The strain-gradient CP constitutive formulation of Dunne et al. [25] is adopted for this study. The equations used in the formulation describe the movement of mobile dislocations, or dislocation glide, through the crystal lattice, with the application of stress. Hardening occurs due to the presence of immobile dislocations, including both statistically-stored dislocations (SSDs) and GNDs, which behave as obstacles in the path of mobile dislocations. The presence of GNDs introduces the strain-gradient effect into the model, as shown below. The schematic of Fig. 2 shows the mechanism proposed here to explain the role of the development of GNDs in causing a grain size effect on fatigue behaviour. This schematic is necessarily a simplistic 2D representation of a complex 3D crystallographic phenomena. An arbitrary grain in a polycrystal is hypothesised to experience a spatial gradient in plastic deformation due, for example, to the orientation and geometry of adjacent grains, as illustrated in Fig 2(a). In this case, the plastic deformation in the  $x$ -direction (signified by the  $xx$  component of the plastic deformation gradient,  $F^p$ ) at A is greater than at B, i.e. a gradient in  $F^p_{xx}$  forms in the  $y$ -direction. A simplified view of the hypothesised deformed crystal lattice within this grain is provided in Fig. 2(b). Dislocations of a particular sign must be stored in order to accommodate the curvature in the lattice, consistent with the gradient in plastic deformation. Therefore, these dislocations are geometrically necessary (i.e. GNDs). While the lattice also experiences stretch and additional rotation under applied and/or residual stress, these forms of deformation are elastic. From Fig. 2(b), the density of GNDs is dependent on the length of the lattice,  $L$ , over which the gradient in plastic deformation exists, as the same number of GNDs are required for a given change in plastic deformation, regardless of the distance over which the change takes place. Two grains under the same applied loading field, in an identical scaled microstructure morphology, will develop GND densities dependent on their respective grain sizes,  $d_1$  and  $d_2$ , as shown in Fig. 2(c). The same

number of GNDs must form along the  $d_2$  dimension of the finer grain as along the  $d_1$  dimension of the coarser grain. Hence, GND densities are higher in finer-grained materials, resulting in increased hardening, and thus, reduced cyclic plasticity.

As the calculation of GND densities is dependent on spatial gradients of deformation, the CP equations are implemented in a user-element subroutine (UEL) in Abaqus to provide access to the necessary element information. The UEL implementation of Dunne et al. [25] is used here. Deformation of the crystal lattice is described in the formulation using a deformation gradient,  $\mathbf{F}$ , with elastic and plastic components:

$$\mathbf{F} = \mathbf{F}^e \cdot \mathbf{F}^p \quad (1)$$

The second Piola-Kirchoff stress,  $\mathbf{S}$ , is used in the implementation, to facilitate large deformation computations. The stress-strain relation is defined as:

$$\mathbf{S}^e = \mathbf{D}_R \mathbf{E}^e \quad (2)$$

where  $\mathbf{D}_R$  is the fourth order elasticity tensor referred to the reference frame,  $\mathbf{E}$  is the Green strain tensor and superscript 'e' denotes variables evaluated at an intermediate frame. Cubic elastic constants are used to construct  $\mathbf{D}_R$ , owing to the fcc structure of the L605 lattice. The second Piola-Kirchoff stress is calculated from the Cauchy stress by:

$$\mathbf{S}^e = \det(\mathbf{F}^e) \mathbf{F}^{e-1} \boldsymbol{\sigma} \mathbf{F}^{e-T} \quad (3)$$

The shear stress on a slip system  $\alpha$  is defined as a function of  $\mathbf{S}$ :

$$\tau^\alpha = (\mathbf{s}_0^\alpha \otimes \mathbf{n}_0^\alpha) : \mathbf{S}^e \quad (4)$$

where  $\mathbf{s}_0^\alpha$  and  $\mathbf{n}_0^\alpha$  denote the slip system direction and normal, respectively, evaluated in the undeformed reference frame. The fcc L605 alloy has twelve  $\{111\}\langle 110 \rangle$  slip systems. The plastic velocity gradient can be expressed as:

$$\mathbf{L}^p = \dot{\mathbf{F}}^p \cdot \mathbf{F}^{p-1} = \sum_{\alpha} \dot{\gamma}^{\alpha} \mathbf{s}^{\alpha}_0 \otimes \mathbf{n}^{\alpha}_0 \quad (5)$$

where  $\dot{\gamma}^{\alpha}$  is the slip rate on a slip system  $\alpha$ . The flow rule, relating slip rate to shear stress,  $\tau^{\alpha}$ , on a slip system, is defined by:

$$\left| \dot{\gamma}^{\alpha} = \rho_{SSD,m} b^2 v \exp\left(-\frac{\Delta H}{kT}\right) \sinh\left(\frac{(\tau^{\alpha} - \tau_c) \gamma_0 \Delta V}{kT}\right) \right| \quad (6)$$

where  $\rho_{SSD,m}$  is the mobile SSD density on a slip system,  $b$  is Burger's vector magnitude,  $v$  is the frequency of attempts by mobile dislocations to overcome energy barriers,  $\Delta H$  is the Helmholtz free energy,  $k$  is the Boltzmann constant,  $T$  is the temperature,  $\tau_c$  is the critical resolved shear stress,  $\gamma_0$  is a reference strain and  $\Delta V$  is the activation volume. The flow rule of Eq. (6) is developed from Gibbs creep rate equation [45], as described by Manonukul et al. [46], in which an exponential function, developed by Granato et al. [47], defines the probability of an energy fluctuation at a given temperature that could allow a dislocation to overcome an energy barrier. The Helmholtz free energy is associated with the activation of pinned dislocation jumps, successful or otherwise, utilised by Gibbs, in order to establish average dislocation glide speed. Forward and backward activation events are taken into account by the hyperbolic sine term of Eq. (6). The activation volume, on which the stress field operates, can be defined by:

$$\Delta V = lb^2 \quad (7)$$

where the pinning distance between dislocations,  $l$ , is described as a function of both immobile SSD density,  $\rho_{SSD,i}$ , and GND density,  $\rho_{GND}$ :

$$\left| l = 1/\sum_{\alpha} (\rho_{SSD,i}^{\alpha} + \rho_{GND}^{\alpha})^{1/2} \right| \quad (8)$$

Thus, the final flow rule is defined by:

$$\left| \dot{\gamma}^\alpha = \rho_{SSD,m} b^2 v \exp\left(-\frac{\Delta H}{kT}\right) \sinh \frac{(\tau^\alpha - \tau_c) \gamma_0 b^2}{kT \sqrt{\sum_\alpha (\rho_{SSD,i}^\alpha + \rho_{GND}^\alpha)}} \right| \quad (9)$$

The slip system GND density is defined here as a function of the elastic deformation gradient:

$$\sum_\alpha (\mathbf{b}^\alpha \otimes \boldsymbol{\rho}_{GND}^\alpha) = (\text{curl} \mathbf{F}^s)^T \quad (10)$$

where  $\mathbf{b}^\alpha$  is Burger's vector and  $\boldsymbol{\rho}_{GND}^\alpha$  is comprised of both edge and screw dislocation density components. Eq. (10) is solved via a least squares minimisation scheme, described fully in previous work [25], whereby the sum of the squares of dislocation densities is minimised. An evolution equation for the immobile SSD density, similar to that presented by Evers et al. [48], has been implemented here in the UEL, to account for both accumulation and annihilation of dislocations:

$$\left| \dot{\rho}_{SSD,i}^\alpha = \frac{|\dot{\gamma}^\alpha|}{b} \left[ \sum_\alpha (H^{\alpha\beta} \rho_{SSD,i}^\alpha + H^{\alpha\beta} \rho_{GND}^\alpha) - 2c\gamma_c \rho_{SSD,i}^\alpha \right] \right| \quad (11)$$

where  $H^{\alpha\beta}$  are interaction coefficients describing the mutual immobilisation between dislocations of different slip systems,  $c$  is a constant and  $\gamma_c$  is the critical annihilation distance. The rationale of Ohashi et al. [49] is adopted for assigning  $H^{\alpha\beta}$ ; dislocations on the same slip system and on coplanar slip systems are assumed not to contribute to the mean free path, and thus a coefficient of 0 is assigned, while a coefficient of 1 is assigned for all other combinations.

The temperature,  $T$ , is set at room temperature (293 K) for the CP simulations, while the frequency,  $\nu$ , is set at  $1.0 \times 10^{11} \text{ s}^{-1}$ , chosen to be two orders of magnitude smaller than the Debye frequency [50]. The mobile SSD density,  $\rho_{SSD,m}$ , and the initial immobile SSD density,  $\rho_{SSD,i}^0$ , are both taken to be  $5 \times 10^{10} \text{ m}^{-2}$ , based on the data presented in [15]. The critical

resolved shear stress,  $\tau_c$ , calculated by dividing the yield stress of the material (reported in previous work [30]) by the Taylor factor for an fcc crystal, is taken as 173.5 MPa. The reference strain is taken as a constant at 0.001. The constant,  $c$ , used in Eq. (11), is set at 0.01, within the range suggested by Ohashi et al. [51], while the critical annihilation distance,  $y_c$ , is taken to be  $2. \times 10^{-9}$  m, similar to that reported by Essmann and Mughrabi [52]. The Helmholtz free energy,  $\Delta H$ , is identified via comparison of the cyclic micromechanical FE analyses with experiments. For simulation of tests at room temperature, as in this study, thermal activation is unlikely to be important, so that in fact the rate-sensitivity (relating to  $\Delta H$ ) in the model is negligibly small.

As stated in the introduction, a key aspect of the present work is the prediction of numbers of cycles to crack initiation,  $N_i$ , and the effect of grain size on this. Microstructure-sensitive FIPs are implemented for this purpose in the UEL, based on variables in the CP equations above. The importance of scale compatibility between constitutive model and FIP based-predictive methods has been previously discussed for CP modelling [29,30]. The effective crystallographic slip parameter of Manonukul and Dunne [37], defined by:

$$\dot{p} = \left( \frac{2}{3} \mathbf{L}^p : \mathbf{L}^p \right)^{1/2} ; \quad p = \int_0^t \dot{p} dt \quad (12)$$

has been related to the formation of PSBs in fatigue [2]. Although the method has been used to predict locations of FCI [38], the present work is the first attempt, to the authors' knowledge, to correlate this parameter with crack initiation life within the context of a physically-based length-scale dependent CP constitutive framework. The crystallographic work parameter [39],  $W$ :

$$W = \sum_{\alpha} \int_0^t \tau^{\alpha} \dot{\gamma}^{\alpha} dt \quad (13)$$

is also investigated here. This energy-based parameter takes into account different aspects of work carried out at a crystallographic level, defined by the terms of Eq. (9). This includes plastic work done by the applied stress field, due to  $\tau^\alpha$ , work hardening with increase in density of GNDs and immobile SSDs, and activation energy for unpinning of mobile dislocations. Both components of the crystallographic work parameter are affected by GND density; slip rate is directly influenced in accordance with Eq. (9), decreasing with increasing GND density due to increased microstructural barriers to slip, and slip system shear stress increases with GND density as increased energy is required to overcome barriers. In the present work, crack initiation is deemed to correspond to critical values of the FIPs presented,  $p_{crit}$  and  $W_{crit}$ , being reached. Cyclic values of the FIPs (i.e. accumulated over a single stabilised cycle) are used to assess when these critical values are reached, i.e.  $N_i = \frac{W_{crit}}{W_{cyc}}$

(similar for  $p$ ).

### 3.2. Finite element microstructure geometry

Microscopy data acquired in Section 2 was used for the generation of realistic polycrystal models for the micromechanical FE analyses. Conversion of the grain area distributions extracted from optical microscopy in Section 2.1 to grain volume distributions was required for generation of the 3D FE geometries. A hexagon and rhombic-dodecahedron were assumed to represent 2D and 3D grains, respectively, as shown in Fig. 3(a). The common dimension,  $d$  (grain size), allows conversion of hexagonal grain area,  $A$ , to rhombic dodecahedron grain volume,  $V$ , fully defined by the equations:

$$A = \frac{\sqrt{3}}{2} d^2 ; \quad V = \frac{1}{\sqrt{2}} \left( \frac{2A}{\sqrt{3}} \right)^{\frac{3}{2}} \quad (14)$$

This approximation facilitated the extraction of grain volume distributions for the two material conditions from their respective grain area distributions. MATLAB [53] was used to generate 3D Voronoi tessellations, which were superimposed on a voxel mesh to generate polycrystal geometries. A polycrystal model was then identified with grain volume distribution that closely correlated to the measured microstructure distribution for the as-received. This model was then scaled to obtain the heat-treated microstructure geometry

according to average grain volumes of the two material conditions, i.e.  $\frac{(V_p)_{coarse}}{(V_p)_{fine}} = \frac{(V_g)_{coarse}}{(V_g)_{fine}}$ ,

where  $V_p$  and  $V_g$  represent FE polycrystal and average grain volumes, respectively.

Comparison of the experimental and sample FE model grain volume distributions can be seen in Figs. 3(b) and (c) for the as-received and heat-treated materials, respectively. Twin boundaries have not been included in the polycrystal FE geometries for this study.

While SEM did not reveal precipitates in the heat-treated material, precipitates were observed in the as-received material. Thus, precipitates have been incorporated into the FE model of the as-received material in order to take into account their effect, additional to the effect of grain size, on fatigue performance. A seven-element unit, composed of a single precipitate element surrounded by six CoCr matrix elements, was developed for this purpose. The FE geometry for the as-received material can be seen in Fig. 3(d), along with the seven-element unit, which slots into the space of a regular element in the mesh. The unit was inserted randomly into the mesh, at a sufficient number of locations to maintain measured precipitate volume fraction. The precipitates were assumed to be tungsten carbides, based on the EDX observations, and were accordingly assigned a high Young's modulus of 714 GPa [54].

Each FE polycrystal comprised 28 crystallographic grains. The mesh for the heat-treated condition consisted of 3375 ( $15^3$ ) 20-noded brick elements with polycrystal dimensions of  $(866 \mu\text{m})^3$ . Replacement of normal elements with the seven-element unit for the as-received condition resulted in a mesh composed of 3723 elements (see Fig. 3(d)), with polycrystal dimensions of  $(120 \mu\text{m})^3$ . Mesh refinement was carried out based on a strain-gradient CP mesh sensitivity study of Cheong et al. [20]. The final mesh used here employs an average of 120 elements per grain; results from Cheong et al. [20] indicated that macroscopic polycrystal response showed little sensitivity to mesh refinement above 8 elements per grain for grain sizes greater than  $30 \mu\text{m}$ . Periodic displacement boundary conditions were applied to the polycrystal to simulate macroscopic behaviour. Due to the prohibitively large computational expense associated with cyclic 3D strain-gradient CP FE analyses, a definitive representative volume element (RVE) has not been used here. However, it has been shown [55] that periodic displacement boundary conditions applied to a volume element smaller than an RVE provide a response between the upper and lower limits of the macroscopic response of that material.

The polycrystal FE analyses used the strain-gradient CP constitutive model to simulate LCF loading of the as-received and heat-treated materials at the two experimental strain ranges of  $\pm 0.5\%$  and  $\pm 1.0\%$ , until stabilisation of the cyclic stress-strain response. In order to predict microstructure-induced results, three realizations of random crystallographic orientation distributions, as represented by the inverse pole figures of Fig. 3(e), are presented for each strain range and material condition. Assignment of random orientations corresponds to a lack of crystallographic texture, corroborated by the EBSD maps of Fig. 1(b).

## **4. Results**

### **4.1. LCF testing**

The fine grain (as-received) material was found to exhibit superior fatigue behaviour for both applied LCF strain ranges. The stress range history of the two materials can be seen in Fig. 4, where cyclic stress amplitudes ( $\Delta\sigma/2$ ) of the fine grain material are approximately 100 MPa greater than that of the coarse grain (heat-treated) material across both applied strain ranges.

The measured total and plastic strain- life data is shown in Figs. 5 (a) and (b), respectively, including additional results from previous work by the authors [30] for the as-received material at applied strain ranges of  $\pm 0.8\%$  and  $\pm 1.2\%$ . A Coffin-Manson fit for the as-received material is also provided in Fig. 5(b). The total strain data of Fig. 5(a) shows that the coarse grain (heat-treated) material exhibits lower fatigue life. However the fine and coarse grain material data points appear to fall on the same Coffin-Manson curve. This demonstrates increased hardness and reduced cyclic plasticity of the fine grain material condition, and suggests that the material exhibits the same relationship between plastic strain and fatigue life for the two grain sizes.

### **4.2. Micromechanical simulations**

The polycrystal FE simulations are used to identify the Helmholtz free energy,  $\Delta H$ , for the strain-gradient CP constitutive model, via comparison of the predicted and measured responses, for the as-received material, using a least squares objective function. All other material parameters are based on physical considerations, as described in Section 3. The complete set of constitutive constants used in the strain-gradient CP formulation is provided in Table 1.

GND density distributions from the CP LCF simulations are presented for a sample microstructure realization in Fig. 6, for both grain sizes, for the two strain ranges. Clearly, significantly higher  $\rho_{GND}$  values are predicted for the fine grain cases. The average  $\rho_{GND}$  distribution is an order of magnitude higher for the fine grain material. A comparison of the predicted and experimental stabilised stress-strain hysteresis loops for one microstructure realization (one random crystallographic orientation set) is shown in Fig. 7; excellent agreement is achieved generally. Cyclic stress range data for experiments and simulations is compared in Fig. 8, including results for all three microstructure realizations. Significantly lower stress ranges are clearly predicted for the coarse grain material.

The measured evolution of cyclic maximum stress response is used here to compute the evolution of fatigue damage and, hence, identify the experimental number of cycles to FCI,  $N_i$ .  $N_i$  is considered to occur at a critical damage  $D_c$ . A high probability exists of FCI occurring at the free surface for the LCF regime [1,56]. Therefore  $D_c$  is selected based on the ratio of cross-sectional area of the specimen compromised by initiation of a crack with depth equal to the standard element size (from the FE polycrystal models) in each repeated unit at the free surface of the fatigue specimen. This leads to a value for  $D_c$  of 0.0125. Experimental damage curves are thus computed for each test, as shown in Fig. 9, using the relation

$$D = 1 - \frac{\sigma}{\sigma_{max}},$$

based on the effective stress damage concept [57], where  $\sigma$  is the cyclic

maximum stress and  $\sigma_{max}$  is the maximum value of  $\sigma$  for each test. The critical values of the FIPs,  $W_{crit}$  and  $p_{crit}$ , are calibrated against  $N_i$  for the fine grain material at the  $\pm 1.0\%$  strain range, where  $W_{crit} = W_{cyc} N_i$  (similar for  $p_{crit}$ ). Maximum cyclic values of the microstructure-sensitive FIPs,  $W_{cyc}$  and  $p_{cyc}$ , are extracted from the micromechanical LCF simulations. The

resulting identified values for  $W_{crit}$  and  $p_{crit}$  are  $9.19 \times 10^4$  MJ m<sup>-3</sup> and 164.3, respectively. Predictions of  $N_i$  for the other grain size-strain range combinations using these critical values, along with the calibrated case, are shown in Fig. 10.  $W$  and  $p$  both clearly capture the decrease in  $N_i$  for the coarse grain material for a given applied total strain range.  $W$  predicts significantly more accurately than  $p$  for all validation cases.

## 5. Discussion

The as-received, fine-grained material exhibits superior fatigue performance than the heat-treated material. The coarse-grained, heat-treated material exhibits lower stress ranges and shorter lives for a given applied strain range, as seen in Figs. 4 and 5(a), respectively. Interestingly, data points for the coarse- and fine-grained materials essentially lie on the same Coffin-Manson line, as shown in Fig. 5(b). It can be postulated that this is due to the increased hardening and thus reduced cyclic plasticity, experienced by the fine-grain material due to the presence of GNDs. In contrast with this, Morrison and Moosbrugger [3] reported differing Coffin-Manson curves for fine and coarse grain nickel (with similar grain sizes to those used here). However, data points provided in the LCF region investigated here show little difference in Coffin-Manson trend. The work of Morrison and Moosbrugger suggests that with further testing towards the HCF regime the Coffin-Manson curves of the fine and coarse grain materials will begin to diverge.

The cyclic hysteresis loops of Fig. 7 clearly show the ability of the strain-gradient micromechanical framework to capture the grain size effect in fatigue. A decrease in stress range is seen with increase in grain size in Figs. 7 and 8. The increased hardening of the fine grain material can be explained by the increased build-up of GNDs. The differences in GND densities of Fig. 6, due to grain size, corroborates the mechanism of GND formation due to

spatial strain gradients proposed in Fig. 2. The authors are not aware of any published measurements of GND density for the present material, particularly after cyclic loading; however, Littlewood and Wilkinson [8] have measured GND densities in Ti-6Al-4V following cyclic loading, and showed that the range was between  $10^{10}$  and  $10^{16}$   $\text{m}^{-2}$ . The predicted values of Fig 6. lie within this range. The influence of hardening due to GNDs on fatigue behaviour is dependent on the relative densities of GNDs and immobile SSDs, as given by Eq. (9). For the coarse grain simulations, the ratio of GND to immobile SSD average densities ranges from 0.35 to 1; for the fine grain simulations, the range is from 2.5 to 4.1. This indicates that while a further decrease in grain size will result in a greater influence of GNDs, as expected, on the other hand, an increase in grain size will result in negligible further deterioration in fatigue performance. This is due to GND densities dropping further below immobile SSD densities and, thus, becoming negligible. This is consistent with the findings of Fleck et al. [15], who showed that strain-gradient effects are most influential in polycrystals for grain sizes of less than 20  $\mu\text{m}$ .

Although both microstructure-sensitive FIPs successfully predict the trend of fatigue performance for the two material conditions (Fig. 10), i.e. higher  $N_i$  for the fine grain material, the crystallographic work parameter,  $W$ , is significantly more accurate. This is corroborated by the approach of Sangid and co-workers [32–34], which predicts crack initiation in a PSB spanning a grain based on minimisation of a summation of energy terms, describing work carried out in the formation of the slip band and extrusions at the intersection with the grain boundary. The  $W$  parameter used in this work does not operate on the assumption of a PSB spanning a grain, but predicts FCI at the point of maximum crystallographic work. However, courtesy of the slip rule in Eq. (9), it incorporates components of energy similar to terms used in the approach of Sangid and co-workers, such

as the applied stress field, work hardening due to immobile dislocation build-up and unpinning of immobile dislocations for glide. Other energetic mechanisms are omitted by the FIP, including dislocation activity explicitly at the grain boundary (i.e. dislocation nucleation and formation of extrusions) and the interruption of lattice stacking sequence by mobile dislocations during slip. The Sangid model is a more detailed one, including atomistic simulations for quantifying grain boundary energy terms, based on the analysis of a single slip band in each grain. It is expected that some of the additional terms may have less influence in the CP approach used here, where the highly organised dislocation dipole structures of a PSB and the PSB-grain boundary interface are not explicitly modelled.

While it may be postulated that the data of Fig. 5(b) indicates that the Coffin-Manson relation can predict total fatigue life for a material across multiple grain sizes, it is important to note that a Coffin-Manson life prediction (for non-laboratory conditions) is dependent on the predicted cyclic plastic strain range and, thus, the constitutive model. The strain-gradient model presented here can clearly be used effectively for multiple grain sizes in conjunction with the Coffin-Manson relation. However, use of this approach with a definitive RVE polycrystal would not produce scatter in life predictions, as this is a bulk material prediction. Microstructure-sensitive FIPs offer the benefit of capturing localised effects, where FCI is predicted to occur at peaks in FIP distributions, present due to microstructural inhomogeneity. Thus, the combination of microstructure-sensitive constitutive model and predictive methods facilitates capture of scatter in life predictions and provides a statistical basis for fatigue design.

It can be seen from the as-received models in Fig. 6 that peaks in  $\rho_{GND}$  distributions often occur near precipitates. To investigate the effect of precipitates on fatigue performance, a

polycrystal model for one microstructure realisation of the as-received material without precipitates was analysed for the two strain ranges. The results indicate that precipitates have a negligible effect on macroscopic hysteresis behaviour of the as-received material. Changes in predictions of  $N_i$  upon removal of precipitates for the two FIPs and the two strain ranges are provided in Table 2. For  $p_{cyc}$ , the predicted effect of precipitate removal on  $N_i$  is small, less than 3%, and does not show a consistent increase or decrease.  $N_i$  is predicted to increase for both strain ranges using  $W_{cyc}$ , with a maximum increase of nearly 13% predicted. However, the higher  $N_i$  values still lie within the range of predictions for the three microstructural realizations of the as-received model with precipitates. Nonetheless, as  $W_{cyc}$  predictions were found to give better correlation with the measured data in Fig. 10, results from these additional simulations predict a bigger difference between fatigue performance of the as-received and heat-treated conditions without the presence of precipitates and, thus, an even larger effect of grain size on FCI life.

This work does not address all types of size effects in fatigue, e.g. some mechanisms relating to intrinsic size effects. For example, a size effect due to build up of dislocations at grain boundaries is not captured. For the bulk material behaviour presented here, statistical size effects and surface constraint effects are not considered to be important. However, such effects may become important for micro-scale applications. Twin boundaries observed in both the as-received and heat-treated microstructures have not been modelled in this study. Simulations of polycrystals with a high frequency of twin boundaries by Sangid and co-workers [32,33], using the energy balance approach for FCI in PSBs, provided strong evidence of FCI occurring in grains with twin boundaries. More recent work presented CP FE simulations investigating the effect of twin boundaries on predicted FIP values [58]. While this work showed that inclusion of twin boundaries in polycrystal simulations results in an

increase in frequency of high FIP values in the vicinity of twin boundaries, the range of maximum FIP values observed appeared largely unaffected. Therefore, while it is anticipated that the inclusion of twin boundaries in the analyses presented here would generally act to reduce predicted crack initiation lives, it is expected that changes in  $N_i$  predictions would be small and predictions for both grain sizes would be equally affected without a change in trend of fatigue behaviour. Alternate candidate constitutive models exist in the literature which could improve hysteresis loop shapes, such as physically-based kinematic hardening formulations, e.g. see [23,48,59]. Also, while the mesh used in this work is sufficiently refined to capture the macroscopic behaviour of a polycrystal [20], further mesh refinement would undoubtedly affect local FCI predictions. However, the purpose of this study was to demonstrate the key role of strain-gradients and GNDs in explaining the grain size effect on fatigue.

The micromechanical framework presented here is directly relevant to analysis of micro-scale devices, where fatigue performance is highly microstructure-dependent, for the assessment and design of device geometry and microstructure. Micromechanics has been used to generate a set of design curves for deployment of cardiovascular stents [12], for example. The present framework can facilitate development of a similar set of design rules for the fatigue of stents, as a function of grain size, crystallographic texture, precipitates, geometry etc.

## **6. Conclusions**

A strain-gradient crystal plasticity methodology has been used to predict the experimentally-observed effect of grain size on cyclic hysteresis response and fatigue crack initiation life for a CoCr alloy, thus demonstrating the key role played by geometrically necessary dislocations in the grain size effect on fatigue. Computational simulations of experimental LCF tests

indicate that, for the CoCr alloy tested, precipitates have negligible effect on hysteresis behaviour and, while, they appear to have an effect on fatigue damage accumulation, leading to crack initiation, it is relatively minor compared to the influence of grain size. A work-based crystallographic parameter was found to be most effective in predicting fatigue crack initiation; this is attributed to the dependence of persistent slip band formation on the dissipation of energy via dislocation activity. The framework presented is applicable to microstructure-sensitive fatigue design of devices and materials.

### Acknowledgements

The authors would like to acknowledge funding from the Irish Research Council under the EMBARK Initiative Scheme and the Irish Centre for High-End Computing (ICHEC) for the provision of computational facilities and support. The EBSD work in this study was carried out at the Materials and Surface Science Institute at the University of Limerick.

### References

- [1] Chan KS. Roles of microstructure in fatigue crack initiation. *Int J Fatigue* 2010;32:1428–47.
- [2] McDowell DL, Dunne FPE. Microstructure-sensitive computational modeling of fatigue crack formation. *Int J Fatigue* 2010;32:1521–42.
- [3] Morrison DJ, Moosbrugger JC. Effects of grain size on cyclic plasticity and fatigue crack initiation in nickel. *Int J Fatigue* 1997;19:51–9.
- [4] Hertzberg RW. *Deformation and fracture mechanics of engineering materials*. 4th ed. J. Wiley & Sons; 1996.
- [5] Miller KJ. Materials science perspective of metal fatigue resistance. *Mater Sci Technol* 1993;9:453–62.
- [6] Connelley T, McHugh PE, Bruzzi M. A review of deformation and fatigue of metals at small size scales. *Fatigue Fract Eng Mater Struct* 2005;28:1119–52.
- [7] Sangid MD. The physics of fatigue crack initiation. *Int J Fatigue* 2013;57:58–72.
- [8] Littlewood PD, Wilkinson AJ. Geometrically necessary dislocation density distributions in cyclically deformed Ti–6Al–4V. *Acta Mater* 2012;60:5516–25.
- [9] Geers MGD, Brekelmans WAM, Janssen PJM. Size effects in miniaturized polycrystalline FCC samples: Strengthening versus weakening. *Int J Solids Struct* 2006;43:7304–21.
- [10] Arzt E. Size effects in materials due to microstructural and dimensional constraints: a comparative review. *Acta Mater* 1998;46:5611–26.

- [11] Gil Sevillano J, Ocaña Arizcorreta I, Kubin LP. Intrinsic size effects in plasticity by dislocation glide. *Materials Science and Engineering: A* 2001;309–310:393–405.
- [12] Grogan JA, Leen SB, McHugh PE. Influence of statistical size effects on the plastic deformation of coronary stents. *J Mech Behav Biomed Mater* 2013;20:61–76.
- [13] Nye JF. Some geometrical relations in dislocated crystals. *Acta Metall* 1953;1:153–62.
- [14] Ashby MF. The deformation of plastically non-homogeneous materials. *Phil Mag* 1970;21:399–424.
- [15] Fleck NA, Muller GM, Ashby MF, Hutchinson JW. Strain gradient plasticity: Theory and experiment. *Acta Metall Mater* 1994;42:475–87.
- [16] Remes H, Varsta P, Romanoff J. Continuum approach to fatigue crack initiation and propagation in welded steel joints. *Int J Fatigue* 2012;40:16–26.
- [17] Zhang M, Zhang J, McDowell DL. Microstructure-based crystal plasticity modeling of cyclic deformation of Ti-6Al-4V. *Int J Plasticity* 2007;23:1328–48.
- [18] Zhang M, McDowell DL, Neu RW. Microstructure sensitivity of fretting fatigue based on computational crystal plasticity. *Tribol Int* 2009;42:1286–96.
- [19] Zhang M, Neu RW, McDowell DL. Microstructure-sensitive modeling: Application to fretting contacts. *Int J Fatigue* 2009;31:1397–406.
- [20] Cheong KS, Busso EP, Arsenlis A. A study of microstructural length scale effects on the behaviour of FCC polycrystals using strain gradient concepts. *Int J Plasticity* 2005;21:1797–814.
- [21] Han C-S, Gao H, Huang Y, Nix WD. Mechanism-based strain gradient crystal plasticity—I. Theory. *J Mech Phys Solids* 2005;53:1188–203.
- [22] Ma A, Roters F, Raabe D. A dislocation density based constitutive model for crystal plasticity FEM including geometrically necessary dislocations. *Acta Mater* 2006;54:2169–79.
- [23] Kuroda M, Tvergaard V. On the formulations of higher-order strain gradient crystal plasticity models. *J Mech Phys Solids* 2008;56:1591–608.
- [24] Counts WA, Braginsky MV, Battaile CC, Holm EA. Predicting the Hall–Petch effect in fcc metals using non-local crystal plasticity. *Int J Plasticity* 2008;24:1243–63.
- [25] Dunne FPE, Kiwanuka R, Wilkinson AJ. Crystal plasticity analysis of micro-deformation, lattice rotation and geometrically necessary dislocation density. *Proc R Soc A* 2012;468:2509–31.
- [26] Smith KN, Watson P, Topper TH. A Stress-Strain Function for the Fatigue of Metals. *J Mater* 1970;5:767–78.
- [27] Brown MW, Miller KJ. A Theory for Fatigue Failure under Multiaxial Stress-Strain Conditions. *Proc Inst Mech Eng* 1973;187:745–55.
- [28] Fatemi A, Socie DF. A Critical Plane Approach to Multiaxial Fatigue Damage Including Out-of-phase Loading. *Fatigue Fract Eng Mater Struct* 1988;11:149–65.
- [29] Sweeney CA, McHugh PE, McGarry JP, Leen SB. Micromechanical methodology for fatigue in cardiovascular stents. *Int J Fatigue* 2012;44:202–16.
- [30] Sweeney CA, O’Brien B, McHugh PE, Leen SB. Experimental characterisation for micromechanical modelling of CoCr stent fatigue. *Biomaterials* 2014;35:36–48.
- [31] Mura T. A theory of fatigue crack initiation. *Mater Sci Eng A* 1994;176:61–70.
- [32] Sangid MD, Maier HJ, Sehitoglu H. The role of grain boundaries on fatigue crack initiation - An energy approach. *Int J Plasticity* 2011;27:801–21.
- [33] Sangid MD, Maier HJ, Sehitoglu H. An energy-based microstructure model to account for fatigue scatter in polycrystals. *J Mech Phys Solids* 2011;59:595–609.
- [34] Sangid MD, Maier HJ, Sehitoglu H. A physically based fatigue model for prediction of crack initiation from persistent slip bands in polycrystals. *Acta Mater* 2011;59:328–41.

- [35] McCarthy OJ, McGarry JP, Leen SB. A finite element study of microstructure-sensitive plasticity and crack nucleation in fretting. *Comp Mater Sci* 2011;50:2439–58.
- [36] McCarthy OJ, McGarry JP, Leen SB. The effect of grain orientation on fretting fatigue plasticity and life prediction. *Tribol Int* 2014.
- [37] Manonukul A, Dunne FPE. High- and low-cycle fatigue crack initiation using polycrystal plasticity. *Proc R Soc Lond A Math Phys Sci* 2004;460:1881–1903.
- [38] Sweeney CA, Vorster W, Leen SB, Sakurada E, McHugh PE, Dunne FPE. The role of elastic anisotropy, length scale and crystallographic slip in fatigue crack nucleation. *J Mech Phys Solids* 2013;61:1224–40.
- [39] Korsunsky AM, Dini D, Dunne FPE, Walsh MJ. Comparative assessment of dissipated energy and other fatigue criteria. *Int J Fatigue* 2007;29:1990–5.
- [40] HAYNES International. HAYNES 25 Alloy 2004.
- [41] Teague J, Cerreta E, Stout M. Tensile properties and microstructure of Haynes 25 alloy after aging at elevated temperatures for extended times. *Metall Mater Trans A* 2004;35:2767–81.
- [42] Davis JR. *Heat-resistant Materials*. ASM International; 1997.
- [43] Poncin P, Gruez B, Missillier P, Comte-Gaz P, Proft JL. L605 precipitates and their effects on stent applications. *Proceedings of the Materials and Processes for Medical Devices Conference*, ASM International; 2005.
- [44] ASTM E606-04. Standard practice for strain-controlled fatigue testing. *Annual Book of ASTM Standards*, West Conshohocken, PA: ASTM International; 2004.
- [45] Gibbs GB. Thermodynamic analysis of dislocation glide controlled by dispersed local obstacles. *Materials Science and Engineering* 1969;4:313–28.
- [46] Manonukul A, Dunne FPE, Knowles D. Physically-based model for creep in nickel-base superalloy C263 both above and below the gamma solvus. *Acta Mater* 2002;50:2917–31.
- [47] Granato AV, Lücke K, Schlipf J, Teutonico LJ. Entropy Factors for Thermally Activated Unpinning of Dislocations. *J Appl Phys* 1964;35:2732–45.
- [48] Evers L., Brekelmans WA., Geers MG. Scale dependent crystal plasticity framework with dislocation density and grain boundary effects. *Int J Solids Struct* 2004;41:5209–30.
- [49] Ohashi T, Kawamukai M, Zbib H. A multiscale approach for modeling scale-dependent yield stress in polycrystalline metals. *Int J Plasticity* 2007;23:897–914.
- [50] Cottrell AH. *An Introduction to Metallurgy*. Edward Arnold; 1979.
- [51] Ohashi T, Barabash RI, Pang JW, Ice GE, Barabash OM. X-ray microdiffraction and strain gradient crystal plasticity studies of geometrically necessary dislocations near a Ni bicrystal grain boundary. *Int J Plasticity* 2009;25:920–41.
- [52] Essmann U, Mughrabi H. Annihilation of dislocations during tensile and cyclic deformation and limits of dislocation densities. *Phil Mag A* 1979;40:731–56.
- [53] MATLAB Release 2010b. The Math Works, Inc., Natick, Massachusetts, United States; 2010.
- [54] Connolly P, McHugh PE. Fracture modelling of WC-Co hardmetals using crystal plasticity theory and the Gurson model. *Fatigue Fract Eng Mater Struct* 1999;22:77–86.
- [55] Jiang M, Alzebdeh K, Jasiuk I, Ostoja-Starzewski M. Scale and boundary conditions effects in elastic properties of random composites. *Acta Mech* 2001;148:63–78.
- [56] Przybyla CP, McDowell DL. Microstructure-sensitive extreme-value probabilities of high-cycle fatigue for surface vs. subsurface crack formation in duplex Ti–6Al–4V. *Acta Mater* 2012;60:293–305.
- [57] Lemaître J. *A course on damage mechanics*. 2nd ed. Springer; 1996.
- [58] Castelluccio GM, McDowell DL. Effect of annealing twins on crack initiation under high cycle fatigue conditions. *J Mater Sci* 2013;48:2376–87.

- [59] Geers MGD, Brekelmans WAM, Bayley CJ. Second-order crystal plasticity: internal stress effects and cyclic loading. *Model Simul Mater Sci Eng* 2007;15:S133–S145.

## Figure Captions

**Figure 1** (a) Optical micrographs of the as-received material and heat-treated material conditions and (b) EBSD orientation maps for the two material conditions along views both parallel and perpendicular to the central axis of the CoCr bar.

**Figure 2** Schematic of (a) development of spatial gradient of plastic strain in a grain due to the orientation of surrounding grains, (b) formation of a GND in the crystal lattice and (c) storage of different GND densities in grains of different size.

**Figure 3** (a) Idealized representations of grain area and volume for conversion of distributions, comparison of experimental and FE model grain volume distributions for microstructures of (b) the as-received material and (c) the heat-treated material, (d) FE microstructure geometry, including precipitate unit, used for simulations of as-received material and (e) inverse pole figures for each realization of the polycrystal model.

**Figure 4** Experimental stress range histories for LCF tests.

**Figure 5** (a) Total strain-life data, and (b) plastic strain-life data for the LCF tests, with fitted Coffin-Manson curve. Plastic strain range,  $\Delta\varepsilon_p$  is calculated as a function of total strain range  $\Delta\varepsilon$ , stress range,  $\Delta\sigma$ , and Young's modulus,  $E$ :  $\Delta\varepsilon_p = \Delta\varepsilon - \Delta\sigma/E$ .

**Figure 6** Distributions of GND density,  $\rho_{GND}$ , in a cut-away view of the model for one microstructure realization, with crystallographic structure shown at the bottom left for the as-received model.

**Figure 7** Comparison of experimental and simulated stabilised hysteresis loops for one simulated microstructure realization.

**Figure 8** Comparison of experimental cyclic stress-strain curves with FE simulations for three microstructure realizations. Filled symbols indicate experimental data, while open symbols mark micromechanical simulations.

**Figure 9** Experimental damage accumulation curves for the LCF tests.

**Figure 10** Comparison of experimental number of cycles to FCI (taken at a critical damage,  $D = D_c$ ) with FE predictions using the microstructure sensitive FIPs,  $W$  and  $p$ .

Fig. 1  
[Click here to download high resolution image](#)

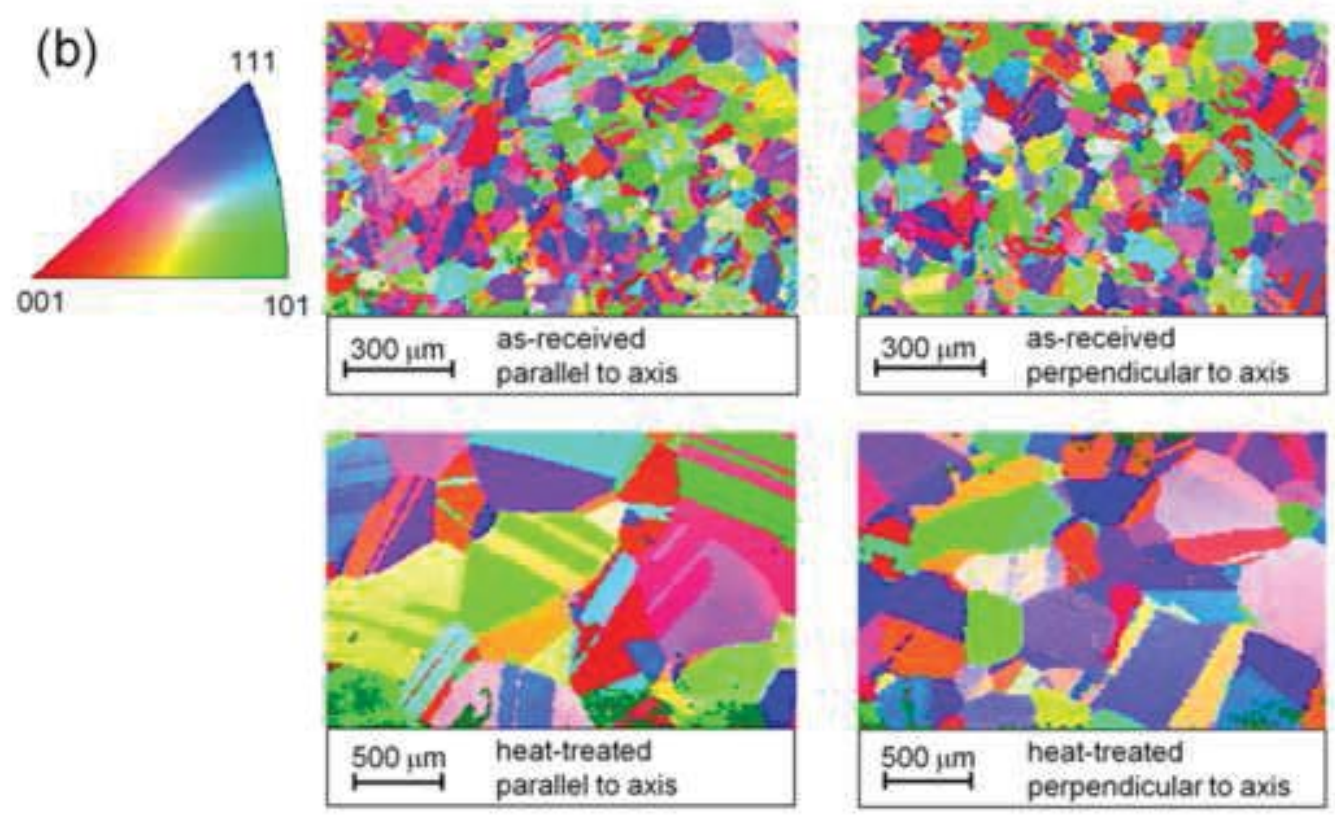
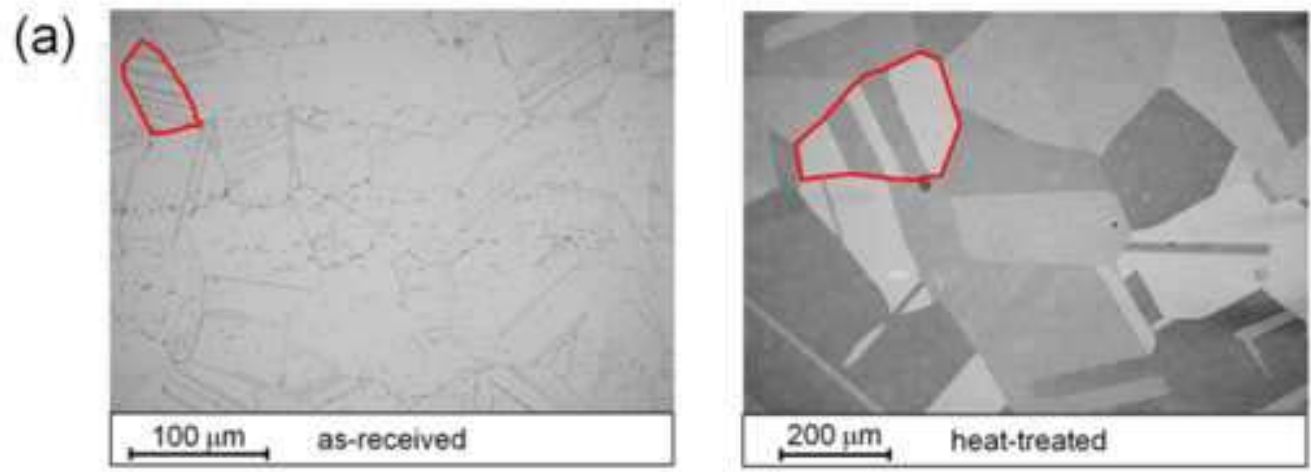


Fig. 2  
[Click here to download high resolution image](#)

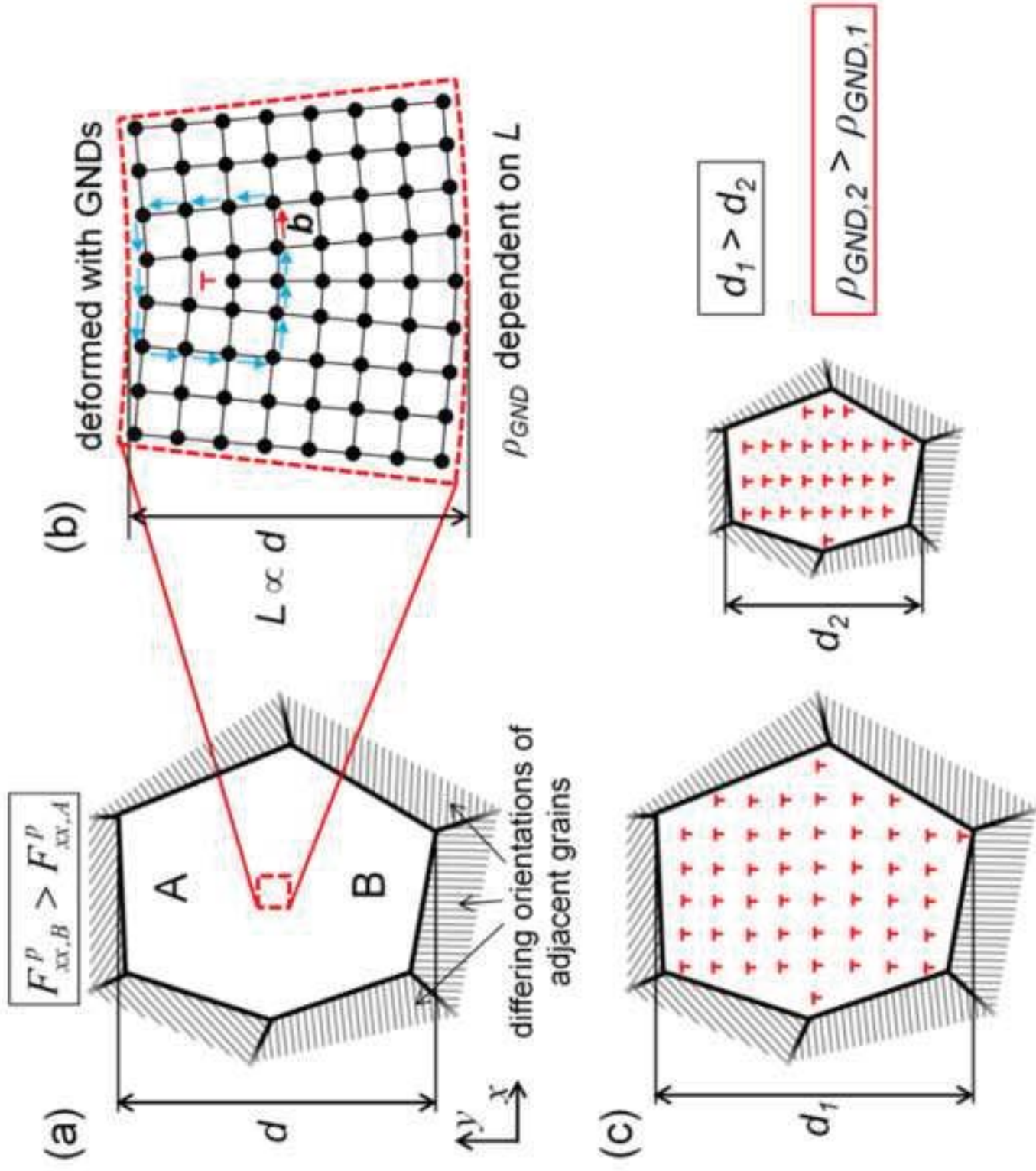


Fig. 3  
[Click here to download high resolution image](#)

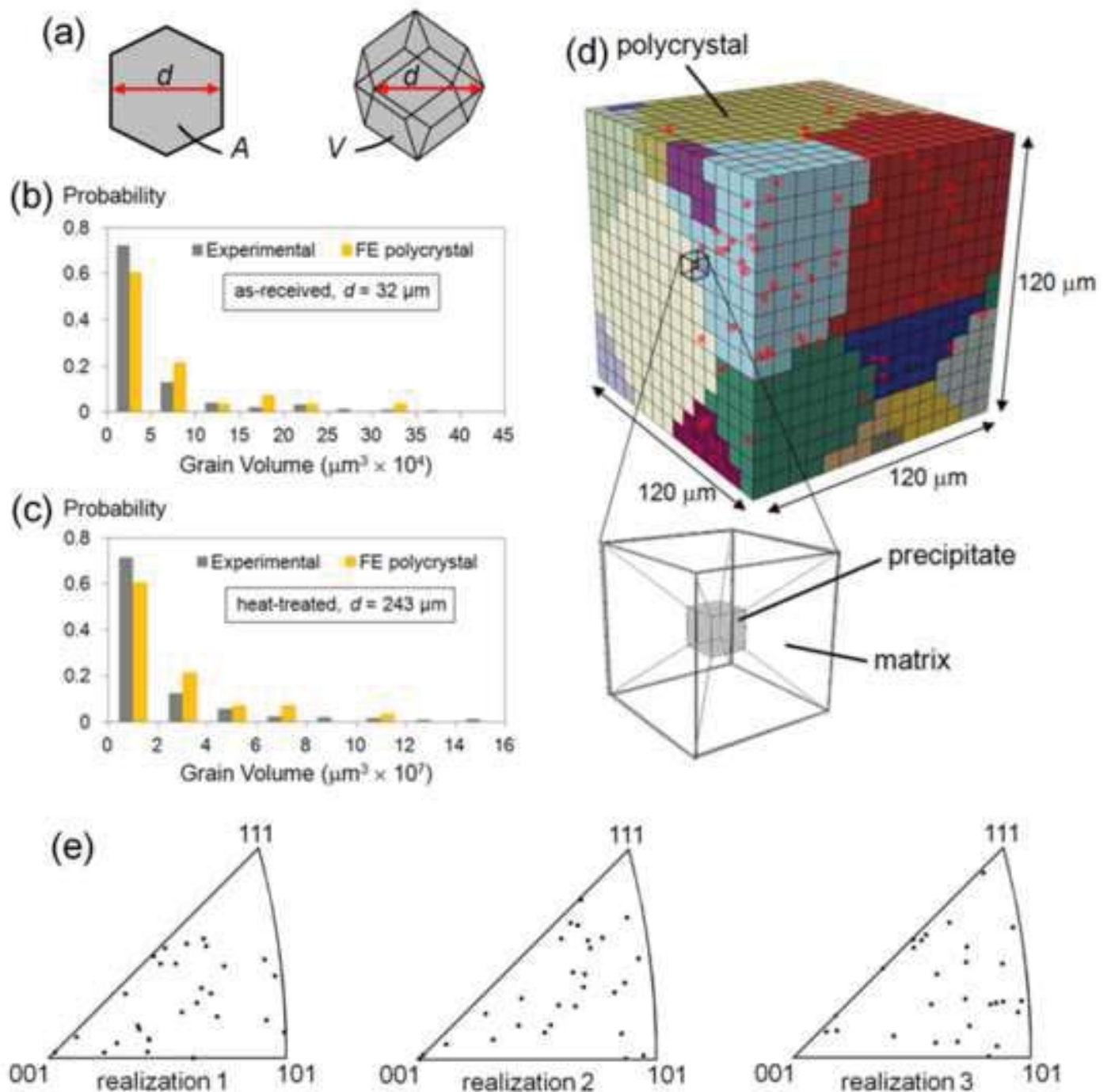


Fig. 4  
[Click here to download high resolution image](#)

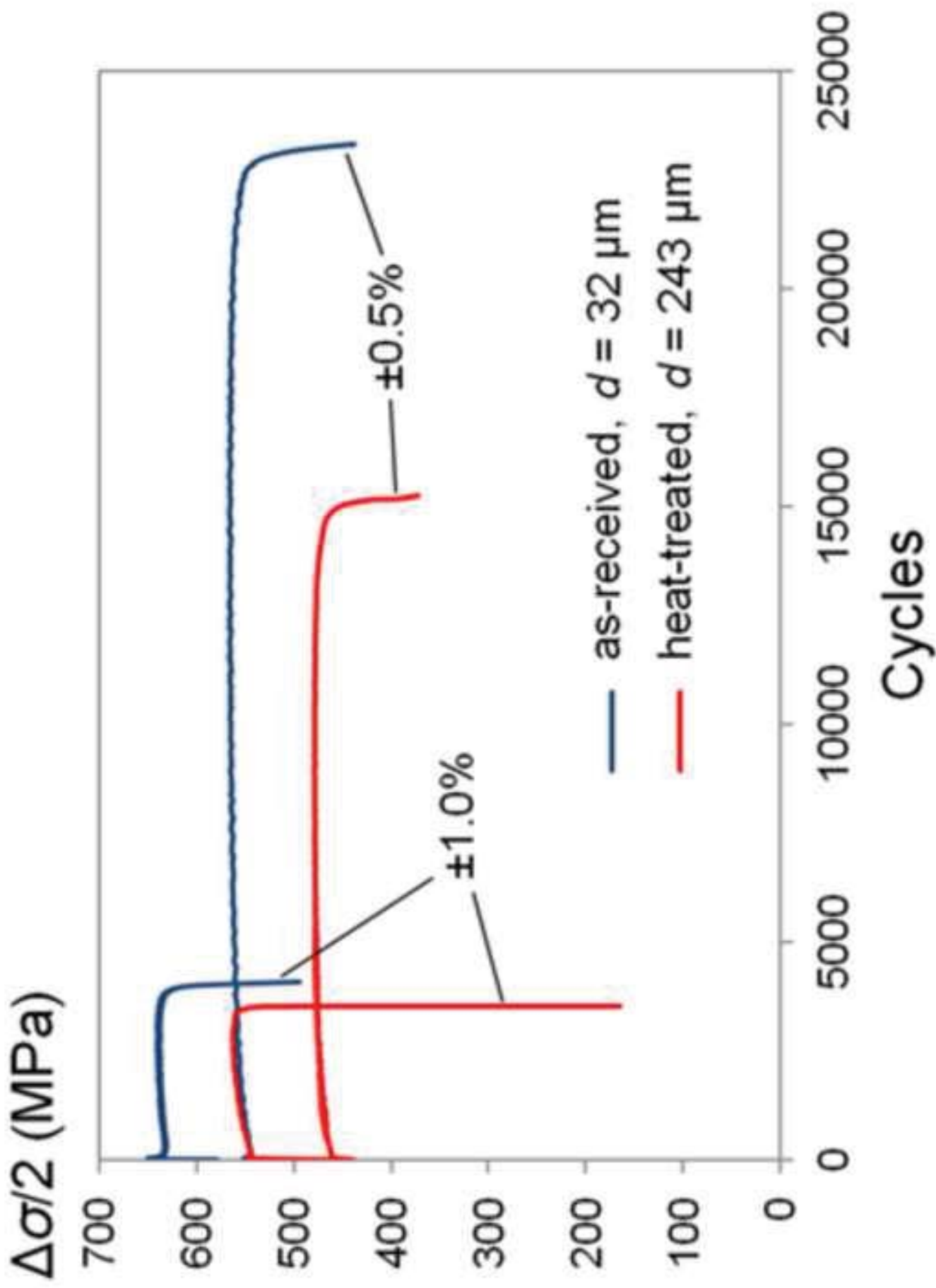


Fig. 5  
Click here to download high resolution image

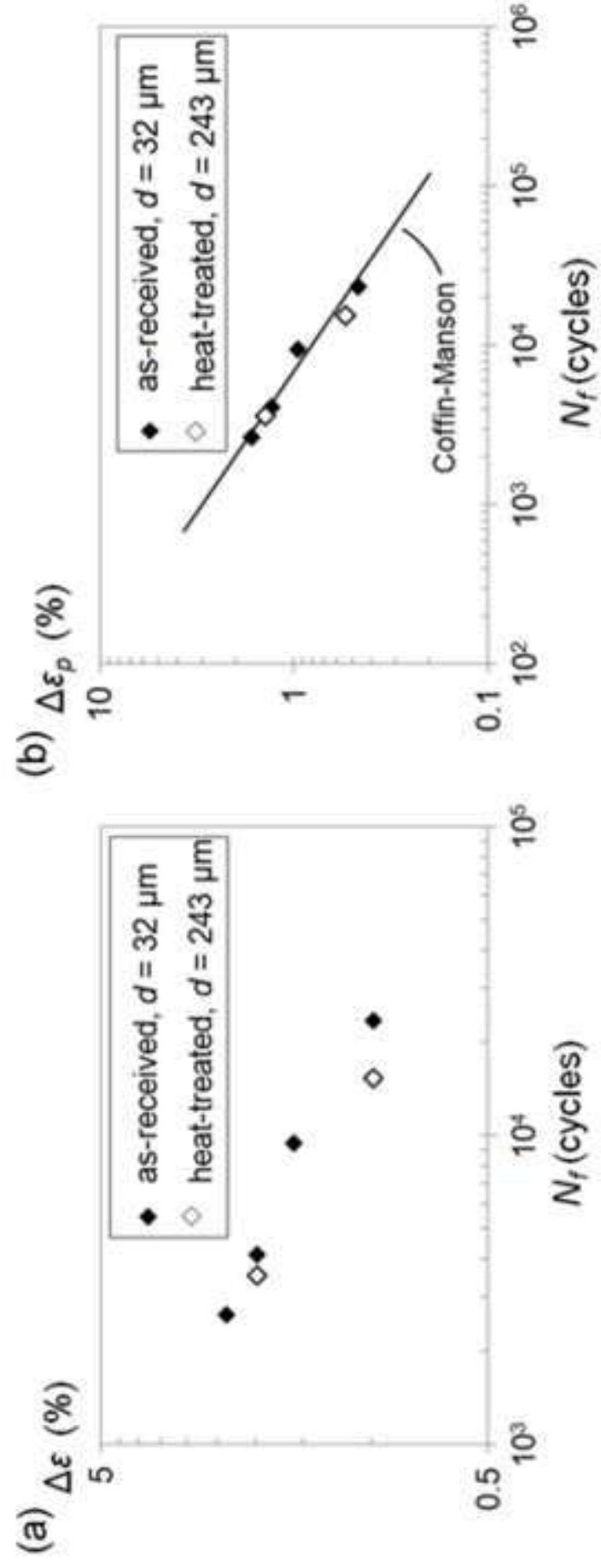


Fig. 6  
[Click here to download high resolution image](#)

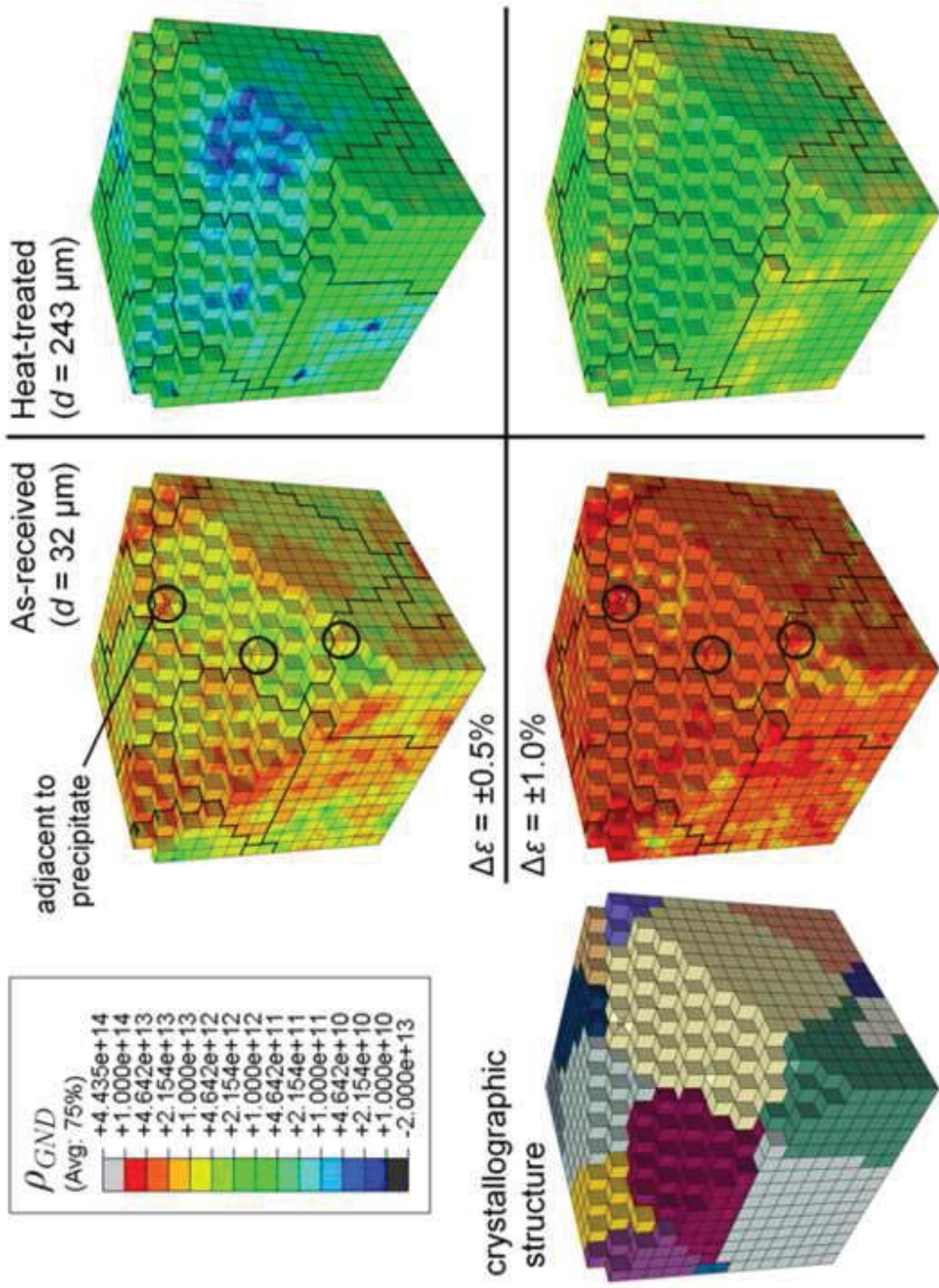


Fig. 7  
[Click here to download high resolution image](#)

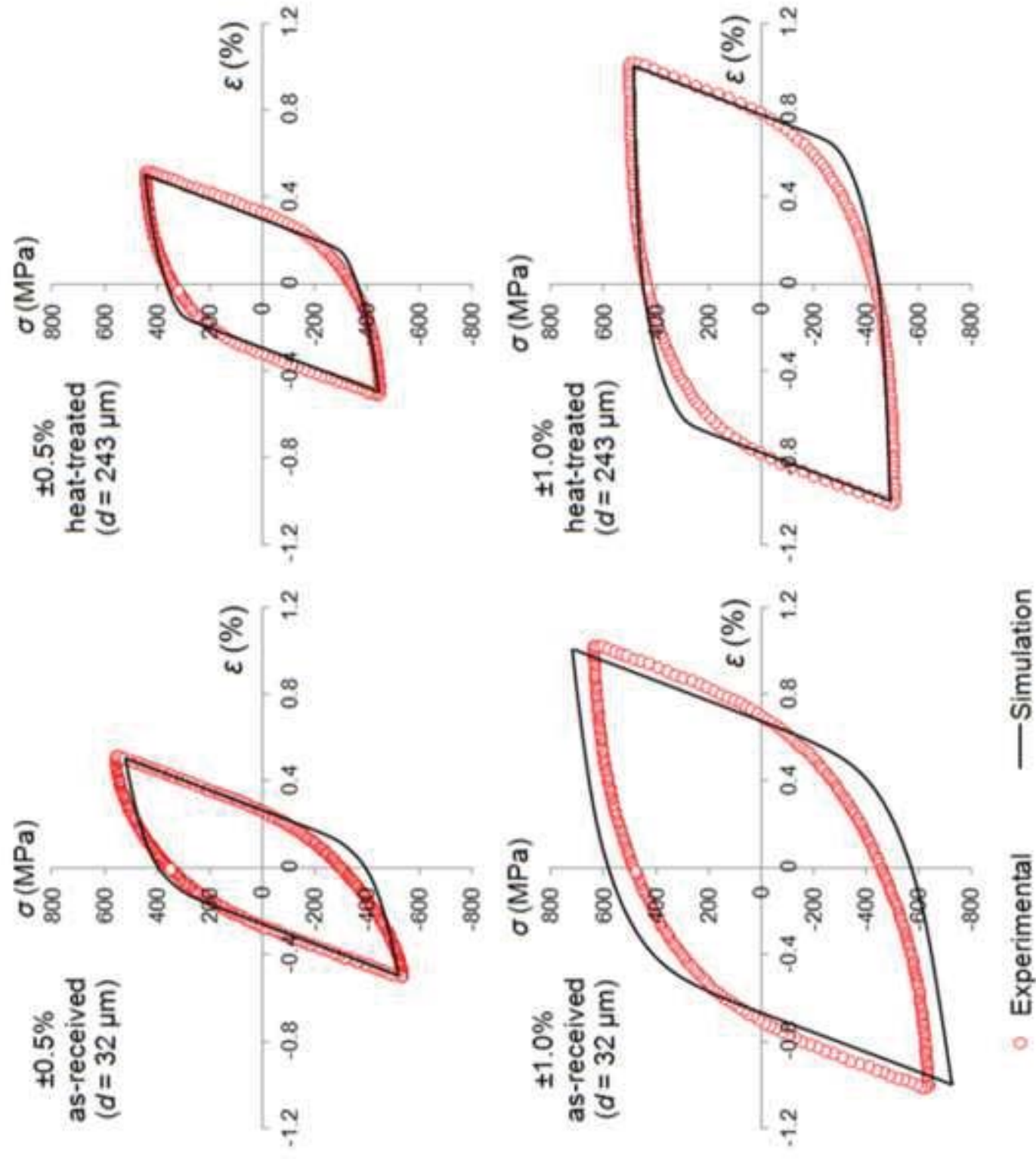


Fig. 8  
[Click here to download high resolution image](#)

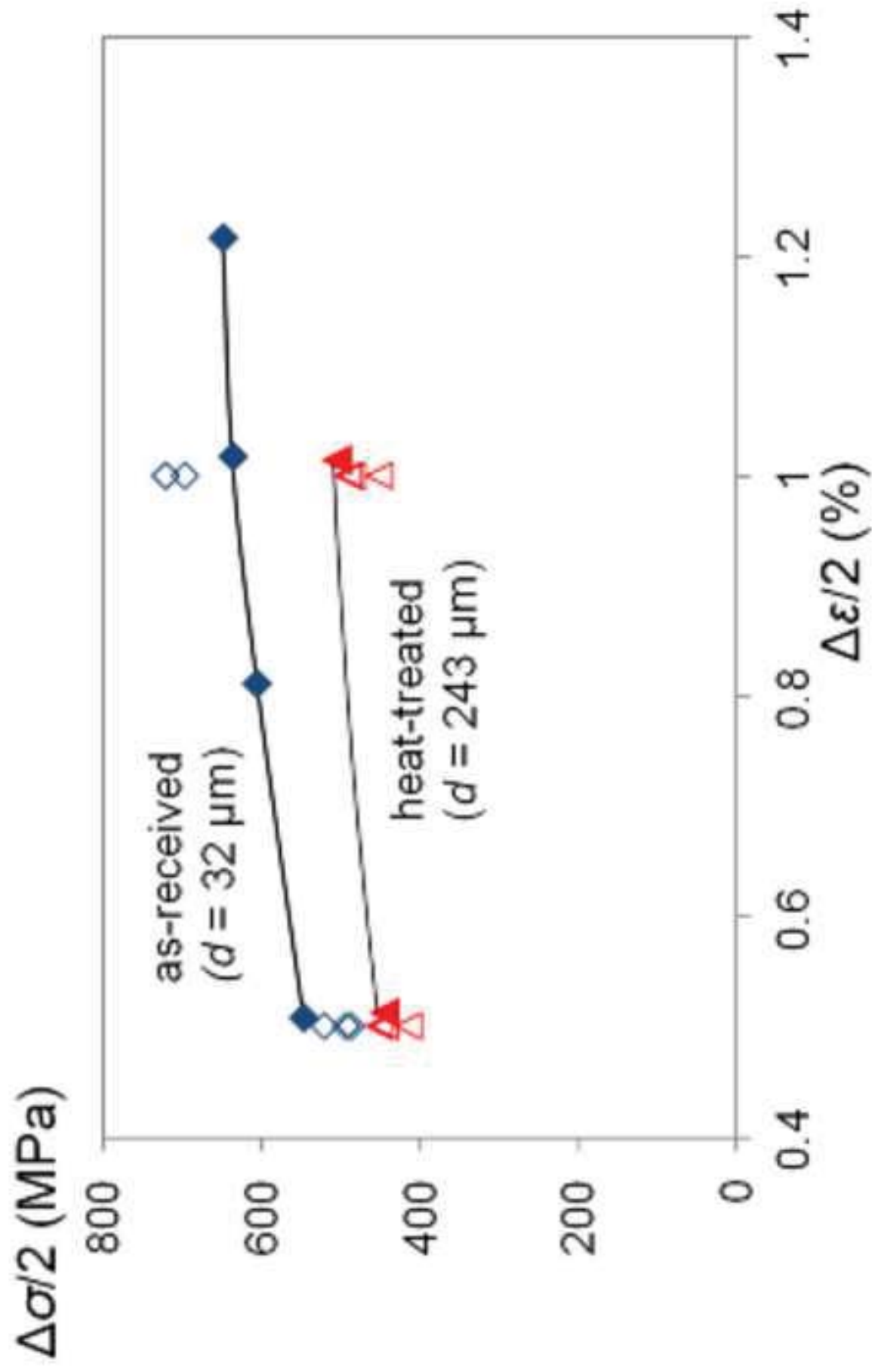


Fig. 9  
[Click here to download high resolution image](#)

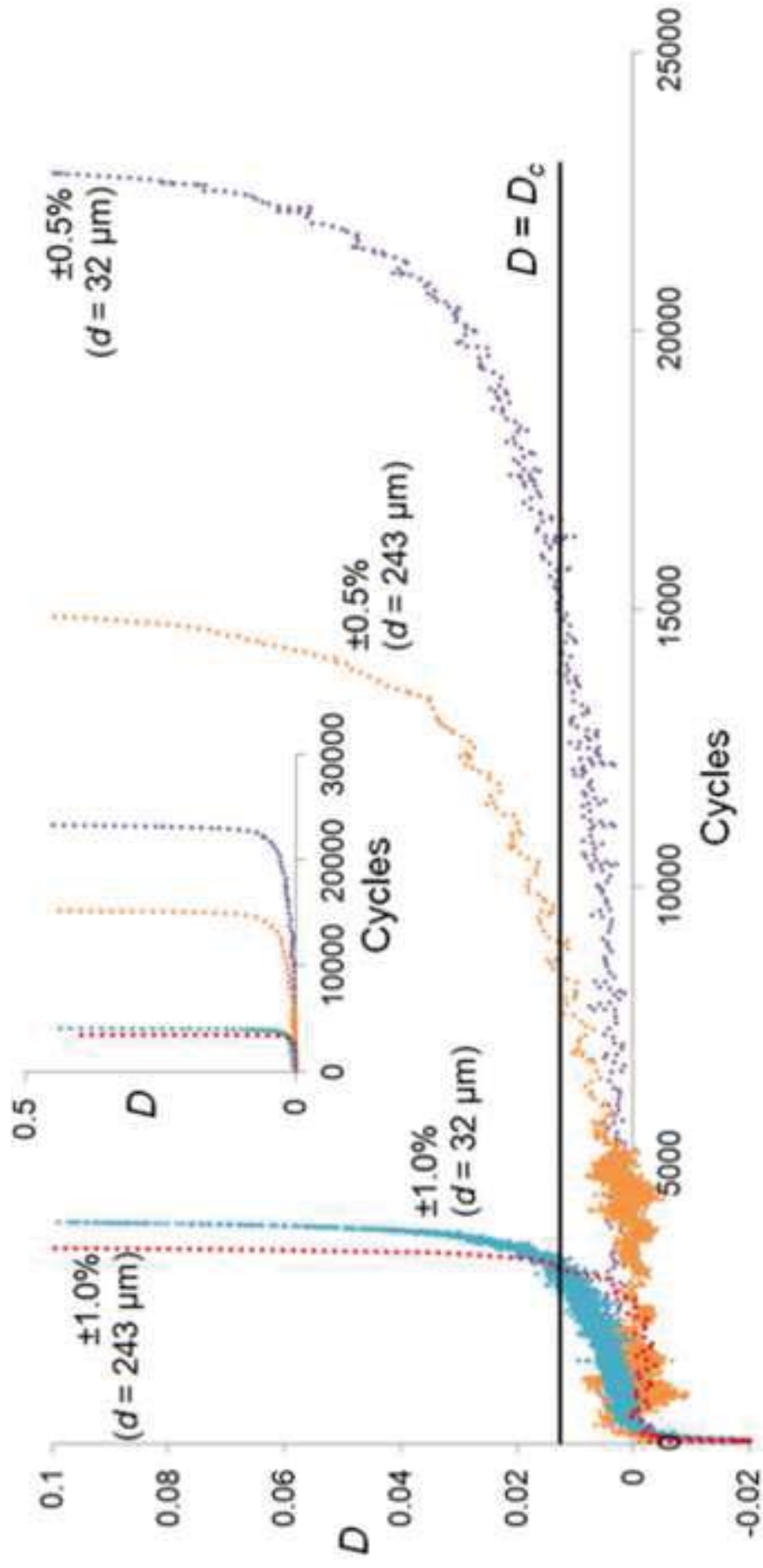
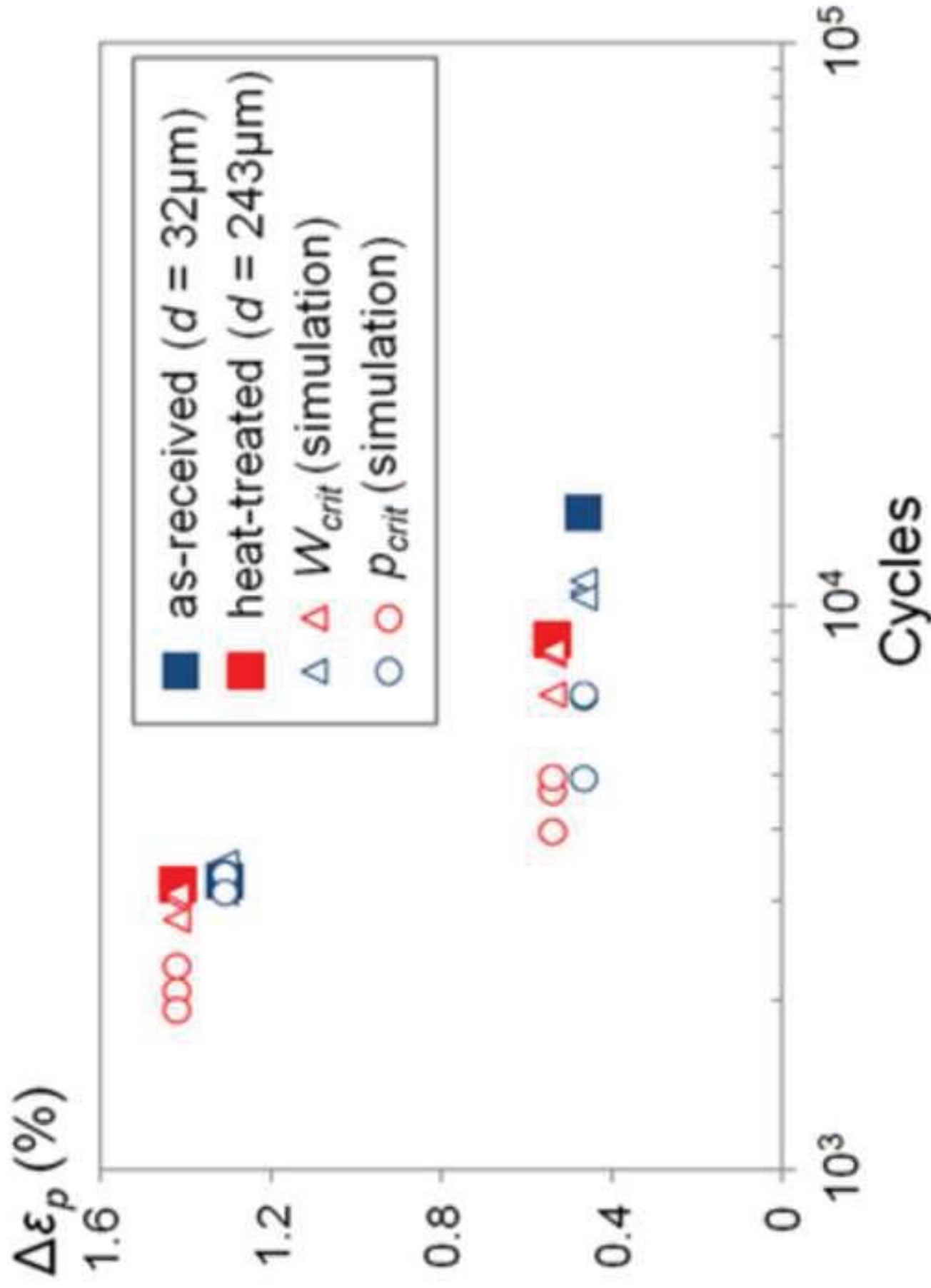


Fig. 10  
Click here to download high resolution image



**Table 1** Strain-gradient CP constants.

$k$	$1.381 \times 10^{-23} \text{ JK}^{-1}$
$T$	293 K
$b$	$2.56 \times 10^{-10} \text{ m}$
$\nu$	$1.0 \times 10^{11} \text{ s}^{-1}$
$\rho_{SSD,m}$	$5 \times 10^{10} \text{ m}^{-2}$
$\rho_{SSD,i}^{\alpha}$	$5 \times 10^{10} \text{ m}^{-2}$
$\tau_c$	173.5 MPa
$\gamma_0$	$1.0 \times 10^{-3}$
$y_c$	$2. \times 10^{-9} \text{ m}$
$c$	0.01
$\Delta H$	$2.85 \times 10^{-20} \text{ J}$

**Table 2** Percentage change in  $N_i$  predictions for one microstructure realisation of the fine grain model, upon removal of precipitates.

$N_i$ (using $W_{eyc}$ )		$N_i$ (using $p_{eyc}$ )	
$\Delta\varepsilon = \pm 0.5\%$	$\Delta\varepsilon = \pm 1.0\%$	$\Delta\varepsilon = \pm 0.5\%$	$\Delta\varepsilon = \pm 1.0\%$
+3.56%	+12.89%	-2.05%	+1.26%